OVERLAY

Journal of Theoretical, Computational and Applied Mechanics

JTCAM

DIAMOND OPEN ACCESS

Identifiers
DOI 10.46298/jtcam.15621
HAL hal-05048399v3

History
Received May 5, 2025
Accepted Oct 15, 2025
Published Feb 25, 2026

Associate Editors
Julien Réthoré
Samuel Forest

Reviewers
Aurélien Doitrand
Raphael Estevez

Open Review
HAL hal-05363319

Supplementary Material
DOI 10.5281/zenodo.17534583.

Licence
CC BY 4.0
©The Authors

Numerical estimation and optimization of the fracture toughness in short-fibre ceramic matrix composites

Sara Jimenez-Alfaro[1], Hyung-Jun Chang[2], Dominique Leguillon[3], and Sébastien Denneulin[4]

[1] Departamento de Mecánica de Medios Continuos y Teoría de Estructuras, Universidad de Sevilla, Sevilla, España
[2] DST Safran Tech, Rue des Jeunes Bois – Châteaufort, Magny Les Hameaux, France
[3] Institut Jean Le Rond d'Alembert, Sorbonne University, Paris, France
[4] Safran Ceramics, Le Haillan, France

Achieving greater engine efficiency by increasing gas temperatures is a key challenge set by the European Commission for the aerospace industry by 2050. However, traditional metal alloys may fail under such extreme conditions. Ceramic matrix composites (CMCs) have emerged as a promising alternative, particularly short-fibre CMCs, which offer enhanced performance in components with complex geometries. This paper presents a novel computational framework to predict the fracture toughness of short-fibre CMCs based on the Coupled Criterion approach. The influence of various composite parameters has been systematically analysed and validated against existing experimental data, demonstrating the model's reliability and potential as a robust design tool for next-generation aerospace applications.

Keywords: coupled criterion, ceramic matrix composites, fracture toughness, aeroengines

1 Introduction

In 2019, the European Commission introduced the European Green Deal, setting ambitious targets to achieve net-zero greenhouse gas emissions by 2050 (European Commission 2019). In response, the aerospace industry has focused on reducing aircraft weight and improving engine efficiency. A key strategy to achieve these goals involves increasing the operating gas temperature from approximately 1700 °C to a target of more than 2000 °C, whereas current metallic alloys used for the gas turbine engine cannot resist a temperature higher than 1300 °C as indicated in (Legerstee 2022). This limitation can be partially addressed through thermal barrier coatings and cooling techniques, although it cannot be completely overcome. This substantial temperature rise presents both challenges and opportunities for material development and engineering innovation.

To achieve this objective, a transition from conventional metal alloys in aircraft engines is essential, as these materials would be unable to perform effectively at the proposed temperatures, even with the application of advanced thermal barrier coatings. Ceramics present a compelling alternative, offering numerous advantages such as low density and exceptional refractory properties, while maintaining mechanical strength at elevated temperatures. Moreover, ceramic matrix composites (CMCs) offer a distinct advantage by enhancing fracture toughness while retaining high thermal stability, low density, and chemical inertness, as explained in (Donald and McMillan 1976). Consequently, they were identified two decades ago as a key material system for improving the thrust-to-weight ratio of high-performance aircraft engines, as indicated in (Ohnabe et al. 1999). Their applications extend beyond aviation, encompassing diverse industrial sectors such as telecommunications, modern electronics, photonics, multifunctional sensors, thermal engines and military technologies, see (Dhanasekar et al. 2022). In addition, it was established that the fracture toughness of the CMCs can be enhanced by introducing weak interfaces between the fibre and the matrix. Then, Martin et al. 1998; Martin et al. 2001

considered crack deflection mechanism at the interface between fibre and matrix as a principal toughening mechanism of the CMCs. This mechanism of microscale cracking in the CMCs was further investigated by many other researchers, see (Gavalda-Diaz et al. 2025) for a recent critical review. While many of these applications predominantly employ long-fibre CMCs, short-fibre CMCs offer an optimal solution for components with complex geometries, such as high-pressure turbine blades. In 2022, a short-fibre CMC was characterised both numerically and experimentally in (Legerstee 2022) as a candidate for the next generation of turbine blades. While the study estimated nearly all the mechanical properties of this material, the fracture toughness of the composite was not numerically analysed, despite its critical importance.

On the other hand, the Coupled Criterion (CC) is a fracture mechanics approach used to predict crack nucleation and initial propagation. In recent years, it has gained recognition for its application to ceramic materials. This method has been applied to describe the concept of tensile strength in polycrystalline ceramics, see (Martin et al. 2018), introducing a novel definition of "inherent" tensile strength applied in numerical models, as described in (Leguillon et al. 2018). Moreover, Jiménez-Alfaro and Leguillon (2021) explained how the CC approach has showcased its versatility in capturing fracture behavior across multiple scales, with noteworthy applications in nacre-like alumina materials, see (Doitrand et al. 2020; Duminy et al. 2023). The CC has also been effectively applied in evaluating the influence of notch radius on fracture toughness in (Picard et al. 2006). Significant progress has been achieved in applying the CC approach to layered ceramics, see (Ševeček et al. 2016), addressing key phenomena such as internal compressive stresses in (Leguillon et al. 2015), edge and tunneling crack formation in (Papšík et al. 2023), and thermal shock damage in (Papšík et al. 2024), among others. Recently, Jiménez-Alfaro and Leguillon (2022) developed a novel computational framework, integrating the Coupled Criterion with the Matched Asymptotics (MA) approach to predict the apparent fracture toughness of glass matrices reinforced with alumina platelets. This innovative model was extended in (Jiménez-Alfaro and Leguillon 2023) to account for the effects of residual stresses and composite volume fraction, offering a more comprehensive understanding of fracture behavior in these materials.

Other experimental and theoretical studies have been applied for explaining the crack path in ceramic matrix composites. Martin et al. (1998) applied an energy criterion for predicting a crack deflection at the fibre-matrix interface. Barsoum et al. (1992) investigated the relationship between microstructural factors and matrix cracking initiation stress in fibre-reinforced ceramic matrix composites. However, the exact process by which these evolve into a macroscopic, fibre-bridged crack remained unresolved.

In this context, this paper aims to apply the Coupled Criterion to estimate the apparent fracture toughness of short-fibre CMCs and to present the predominant toughening mechanisms as a function of the geometrical parameters in the composite. A key aspect of the computational framework developed in this study is its ability to account for the influence of fibre interactions on crack propagation. The paper is organized as follows: Section 2 provides a comprehensive description of the Coupled Criterion. Section 3 details the material properties and the case study applied to illustrate the computational methodology. The main results, including a comparison of numerical predictions with existing experimental data, are presented and discussed in Section 4. Finally, Section 5 summarizes the principal conclusions drawn from this study.

2 The Coupled Criterion

The Coupled Criterion (CC) model enables the prediction of crack nucleation in brittle materials. This criterion is supported by prior experiments on transverse cracking in cross-ply laminates, see (Weißgraeber et al. 2016). According to the CC model first introduced in (Leguillon 2002), two necessary conditions, when met together, are sufficient to predict crack nucleation, as fracture occurs when both are simultaneously satisfied: (i) an energy condition, based on an energy balance, and (ii) a stress condition. In (Jiménez-Alfaro and Leguillon 2023), the two conditions of the CC are summarized considering a structure with N different materials for a 2D case. First, the stress condition is written as a function of the tensile stress $\sigma(s)$ prior to any crack extension, i.e.,

the stress component in the normal direction n highlighted in Figure 1:

$$\bar{\sigma} = \frac{\sigma(s)}{\sigma_c(s)} \geqslant 1, \quad 0 \leqslant s \leqslant \delta l, \tag{1}$$

where s denotes the coordinate along the expected crack path, see Figure 1, and δl is the newly created crack length. The function $\sigma_c(s)$ describes the tensile strength along the expected crack path $0 \leqslant s \leqslant \delta l$,

$$\sigma_c(s) = \sum_{i=1}^{N} \sigma_c^{(i)} \left[H(s - \delta l^{(i-1)}) - H(s - \delta l^{(i)}) \right], \tag{2}$$

H being the Heaviside function and $\delta l^{(0)} = 0$.

Figure 1 Expected crack path in a specimen with a heterogeneous structure made of two materials A and B.

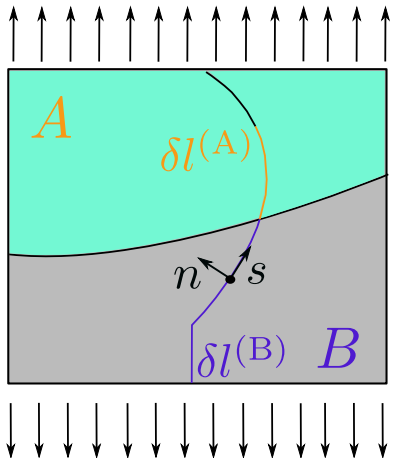

The energy condition for a newly created crack length δl is written in a heterogenous structure as

$$G_{inc} = -\frac{\Delta\Pi_p(\delta l)}{\delta l}, \tag{3}$$

and therefore

$$\frac{G_{inc}}{\overline{G}_c(\delta l)} \geqslant 1, \tag{4}$$

where $\Delta\Pi_p(\delta l)$ is the difference in potential energy between the initial state prior to any crack extension and the final state when a crack of length δl is generated $\Delta\Pi_p(\delta l) = \Pi_p(\delta l) - \Pi_p(0)$. The function $\overline{G}_c(\delta l)$ describes the critical energy release rate along the expected crack path,

$$\overline{G}_c(\delta l) = \frac{\sum_{i=1}^{N} G_c^{(i)} \, \delta l^{(i)}}{\delta l} \tag{5}$$

$\delta l^{(i)}$ being the crack length associated with material (i). Hence, the minimum admissible load for which both Equations (1) and (4) are satisfied determines the crack onset. This, in turn, defines the nucleation length, δl_c, which represents the initial crack jump upon nucleation, within the framework of Finite Fracture Mechanics.

3 Computational framework to estimate the fracture toughness in CMCs

This section presents the computational tool employed to numerically assess the fracture toughness of short fibre ceramic matrix composites (CMCs). Section 3.1 provides an overview of the material properties used, alongside the experimental determination of fracture toughness. Section 3.2 outlines the applied methodology, which utilises the Matched Asymptotics technique

to derive the solution in the vicinity of the crack tip under Mode I loading conditions. This solution is then linked to the composite's fracture toughness through the Coupled Criterion. The proposed tool significantly reduces the computational cost associated with such problems, where fine mesh resolution is necessary to accurately capture the behaviour in the region surrounding the small-scale constituents of the matrix (the short fibres).

3.1 Material

This paper examines two ceramic matrix composites (CMCs) reinforced with short fibres, both of which have been numerically and experimentally characterised in (Legerstee 2022). The first CMC (named in the text as **Material 1**) features a matrix composed of $TiSi_2$ and $MoSi_2$. Notably, $MoSi_2$ undergoes a striking transformation from brittle behaviour at low temperatures to ductile behaviour at elevated temperatures (around 900 °C), making it an ideal candidate for high-pressure turbine blade applications. Complementing this, $TiSi_2$ is strategically incorporated to counteract the oxidation of $MoSi_2$ in air — a well-known degradation phenomenon termed "pest". The composite is further reinforced with silicon carbide (SiC) Hi-Nicalon fibres, selected for their outstanding high-temperature performance and their ability to overcome the oxidation limitations typical of conventional SiC fibres. The second CMC (denoted in the text as **Material 2**) retains the same matrix and fibre composition but introduces a Pyrocarbon (PyC) interphase. This addition significantly enhances the composite's overall resilience and mechanical performance.

The two materials are characterised both numerically, using statistical methods, and experimentally. In both cases, the fibre volume fraction is approximately $V_f \approx 12\,\%$. The fibres exhibit a length range from a minimum of $l_{\min} = 24.41\,\mu\text{m}$ to a maximum of $l_{\max} = 2272\,\mu\text{m}$, while their diameters vary between $t_{\min} = 8.500\,\mu\text{m}$ and $t_{\max} = 53.30\,\mu\text{m}$. Based on statistical distributions, the average fibre length and diameter are determined to be $l_{\text{avg}} = 152.0\,\mu\text{m}$ and $t_{\text{avg}} = 16.67\,\mu\text{m}$, respectively.

Table 1 presents the mechanical properties of the constituents, as reported in (Legerstee 2022). The material properties of the composite are obtained applying the Voigt rule, and depend on the volume fraction. Notably, for the interphase, while the values of σ_c and K_c are experimentally determined for the PyC material, the Young's modulus provided in (Legerstee 2022) corresponds to that of BN, due to confidentiality reasons. For the sake of consistency, this same value is adopted in the present analysis. Notice that the interface between the interphase, the fibre and the matrix is considered strong.

Table 1 Mechanical properties of the constituents of the composite material under study, see (Legerstee 2022).

Constituents	E [GPa]	σ_c [MPa]	K_c [MPa$\sqrt{\text{m}}$]
Fibre	420	1222	1.74
Interphase	20	107	0.35
Matrix	359	200	2.42

It is worth noting that in (Legerstee 2022), a study on the sensitivity of the elastic properties in the three spatial directions is conducted, concluding that the differences are not significant, and thus considering anisotropy is not necessary for this material.

The fracture toughness of the composite is estimated in (Legerstee 2022) using an analytical approximation based on Linear Elastic Fracture Mechanics (LEFM) and experimentally determined through Digital Image Correlation (DIC). In the first one, a shape factor $f(a/W)$ is used,

$$K_{\text{LEFM}} = f\left(\frac{a}{W}\right)\sigma_c\sqrt{\pi a}, \tag{6}$$

where a and W are the notch and the specimen width, respectively, see Figure 2. The tensile strength σ_c of the composite is obtained considering the critical force of the test P_c:

$$\sigma_c = \frac{3P_c(L_e - L_i)}{2eW^2} \tag{7}$$

being e the thickness of the specimen, and L_e, L_i the position of the boundary conditions, see

Figure 2. The shape factor is defined as

$$f\left(\frac{a}{W}\right) = \frac{1.1215}{\sqrt{\left(1-\frac{a}{W}\right)^3}}\left[\frac{5}{8} - \frac{5}{12}\frac{a}{W} + \frac{1}{8}\left(\frac{a}{W}\right)^2 + 5\left(\frac{a}{W}\right)^2\left(1-\frac{a}{W}\right)^6 + \frac{a}{W}\exp\left(-\frac{6.1342\frac{a}{W}}{1-\frac{a}{W}}\right)\right]. \quad (8)$$

The second methodology is based on the well-known Williams´s expansion in (Williams 1952), that defines the elastic solution $u(r,\theta) = K_I r^{0.5} u_I(\theta)$ in the neighbourhood of the Mode I crack tip. The DIC technique is applied to obtain the displacement field at the moment of failure, and therefore $K_c = K_I$. The results are presented in Table 2.

Table 2 Fracture toughness obtained in the composite, as reported in (Legerstee 2022).

Fracture Toughness	K_c^{LEFM} [MPa$\sqrt{\mathrm{m}}$]	K_c^{DIC} [MPa$\sqrt{\mathrm{m}}$]
Material 1	2.80 - 3.45	3.50 - 4.40
Material 2	3.87 - 4.25	5.20 - 6.32

Additionally, the fibre orientation study presented in (Legerstee 2022) reveals that most fibres are aligned within the same plane. This alignment enables the definition of an equivalent 2D problem, akin to the approaches described in (Jiménez-Alfaro and Leguillon 2022; Jiménez-Alfaro and Leguillon 2023).

3.2 Model description to estimate the fracture toughness

The problem addressed in this paper, as illustrated in Figure 2, is inspired by the computational tool developed in (Jiménez-Alfaro and Leguillon 2022; Jiménez-Alfaro and Leguillon 2023). It consists of a 3-point bending test with a pre-existing crack, Γ_c, subjected to Mode I loading conditions. At the crack tip, a fibre is positioned perpendicularly to the crack. The fracture toughness is estimated by studying the crack propagation of Γ_c, considering two possible scenarios: the crack may either penetrate the fibre or deviate along the interface if the first material described in Section 3.1 is considered, or follow the interphase path if the second material is analysed.

To determine this, the CC approach is applied, which requires the elastic solution $U(x_1, x_2)$ in the vicinity of the crack tip. An estimation of this solution is obtained using the quasi-analytical Matched Asymptotics (MA) technique, which is extensively described in (Jiménez-Alfaro et al. 2025). This approach is particularly useful in minimizing numerical errors that may arise when employing very small elements near perturbations. Additionally, it helps reduce the computational complexity of problems involving features such as platelet reinforcements embedded in brittle matrices (Jiménez-Alfaro and Leguillon 2022; Jiménez-Alfaro and Leguillon 2023).

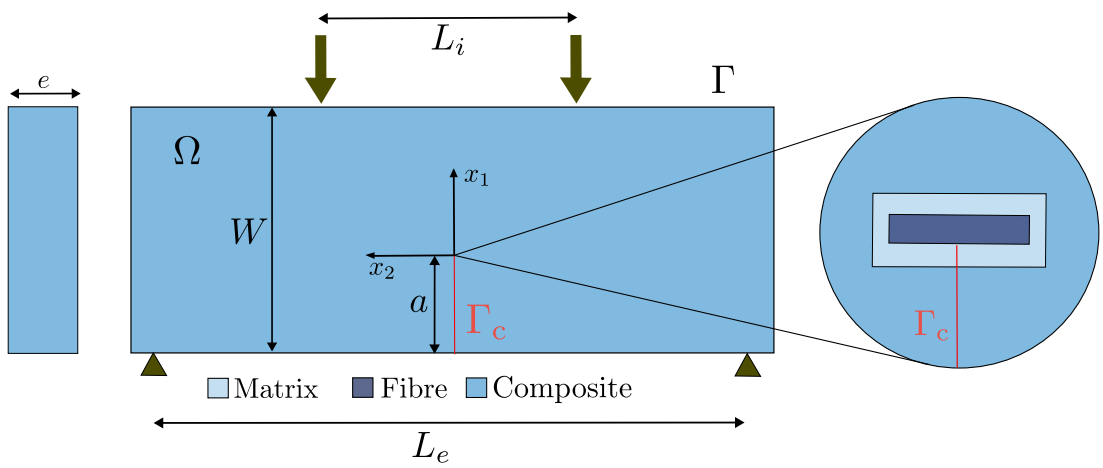

Figure 2 Problem being solved: a 3-point bending test with a pre-existing crack, Γ_c, interacting with a perpendicular short fibre.

In the MAE, the solution $U(x_1, x_2)$ in the vicinity of the tip of Γ_c can be approximated by an inner and an outer expansion. In the outer expansion

$$U(x_1, x_2) = U_0(x_1, x_2) + \text{small perturbation}, \quad (9)$$

where $U_0(x_1, x_2)$ is the solution of the same elastic problem as the one indicated in Figure 2, but assuming that the influence of the short fibre located at the tip of Γ_c is negligible. Hence, the solution can be described by the William's expansion explained in (Williams 1952) that in polar coordinates (r, θ) is written as

$$U_0(x_1, x_2) = U_0(0, 0) + K_I \sqrt{r} U_I(\theta) + \dots \tag{10}$$

K_I being the stress intensity factor and $U_I(\theta)$, the opening shape function for a crack under Mode I, see (Jiménez-Alfaro et al. 2025) for more details.

In the inner expansion, the solution is expressed through a change of variable, where the primary dimensions of the domain are non-dimensionalized by one of the characteristic lengths of the problem. This ensures that the dimensions of the specimen are significantly larger than the selected length scale. In this study, two main parameters are considered: the length (l) and the diameter (t) of the fibre. Hence, the change of variable can be $x_i = l y_i$ or $x_i = t y_i$, respectively. If the problem depicted in Figure 2 is modified by this change of variable, an unbounded domain, Ω_{in}, is obtained, under the condition that the dimensions l and t are much smaller than the specimen's overall dimensions. In this paper, two possible configurations of the inner domain are considered: the one proposed in (Jiménez-Alfaro and Leguillon 2022), shown in Figure 3, and a new configuration that incorporates the effect of the interaction between fibres, as illustrated in Figure 4.

Figure 3 Inner domain with a single fibre. Initial undeformed shape.

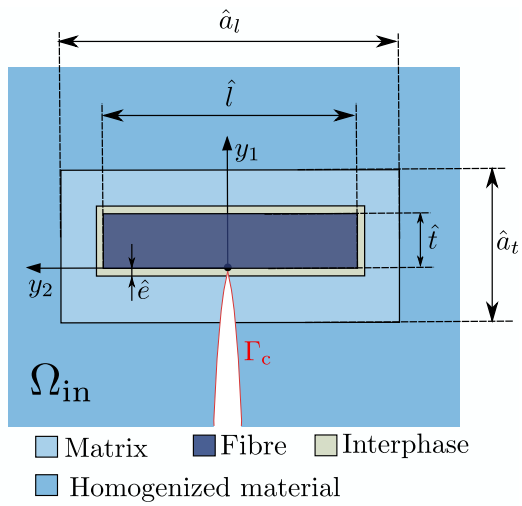

In Figure 3, the parameter $\hat{e}$ represents the thickness of the interphase, e, normalised by the characteristic dimension of the fibre used in the non-dimensionalisation of the inner domain, either l or t. The three geometric parameters l, e, and t are related through a shape factor, $f_e = \frac{lt}{e}$. It is important to note that if the first material is considered, there is no interphase in the composite material, and thus $e = 0$, see Section 3.1. In the proposed model, it is assumed that around the fibre there exists a region of a certain size, free of fibres, and composed solely of the matrix. The size of this region is defined by the fibre volume fraction, V_f, as explained in (Jiménez-Alfaro and Leguillon 2023). For instance, when the change of variable is performed using the fibre diameter, t, the dimensions of this region are

$$\hat{a}_t = \frac{t}{l\sqrt{V_f}}, \quad \hat{a}_l = \frac{1}{\sqrt{V_f}}. \tag{11}$$

The model shown in Figure 4 considers the effect of fibres in proximity to the preexisting crack Γ_c, enabling the study of potential interactions between fibres by modifying the separation distance. Two new parameters are introduced: $\hat{h}_l$ and $\hat{h}_t$, which represent the horizontal and vertical distances between fibres, respectively. The geometric parameters $\hat{a}_l$ and $\hat{a}_t$ in Figure 4 are defined as

$$\hat{a}_l = 3\hat{l} + 2\hat{h}_l + 6\hat{e}, \quad \hat{a}_t = 3\hat{t} + 2\hat{h}_t + 6\hat{e}. \tag{12}$$

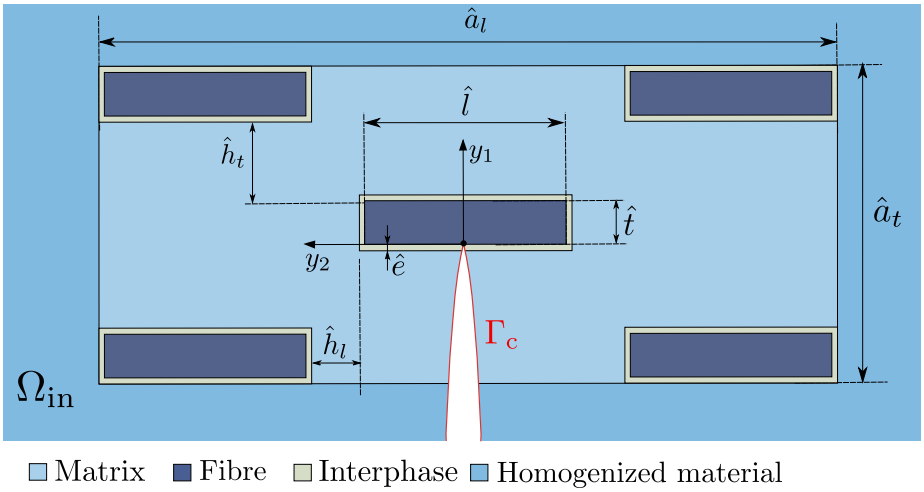

Figure 4 Inner domain with multiple fibres. Initial undeformed shape.

Some restrictions are naturally deduced from the model

$$\hat{a}_l > 0 \quad \text{and} \quad \hat{a}_t > 0, \tag{13}$$

$$\text{if } \hat{h}_l \hat{h}_t > 0 \quad \text{then} \quad \hat{h}_l, \hat{h}_t > 0, \tag{14}$$

$$5\hat{l}\hat{t} = V_f \hat{a}_l \hat{a}_t, \tag{15}$$

$$\hat{a}_l - 2\hat{l} - 6\hat{e} > 0 \quad \text{and} \quad \hat{a}_t - 2\hat{t} - 6\hat{e} > 0. \tag{16}$$

The first restriction, as shown in Equation (13), ensures that the dimensions $\hat{a}_l$ and $\hat{a}_t$ are always positive. The second restriction, expressed in Equation (14), stipulates that one fibre cannot penetrate another in the model. Equation (15) simply reiterates that the definition of the fibre volume fraction must be satisfied. Finally, the last condition, given in Equation (16), is applied to prevent fibres from overlapping in the geometry. It is important to note that these restrictions alone are not sufficient to yield a unique solution for the geometry of the problem, as $\hat{t}$ and $\hat{l}$ remain free parameters. Consequently, we select these two parameters in such a way that they minimise the surface area of the multi-fibre model, which is defined as

$$S(\hat{h}_l, \hat{h}_t) = \hat{a}_l \hat{a}_t = (3\hat{l} + 2\hat{h}_t + 6\hat{e}). \tag{17}$$

Although we use this hypothesis, at the end of this section we will change it to study the influence of $\hat{h}_l$ and $\hat{h}_t$.

As an example, the development of the inner expansion is written below considering the length of the fibre as the characteristic length in the adimensionalization, but a similar development can be obtained with the diameter of the fibre. The inner expansion is therefore defined as

$$U(x_1, x_2) = U(ly_1, ly_2) = F_0(l)V_0(y_1, y_2) + F_1(l)V_1(y_1, y_2) + \cdots \tag{18}$$

The terms of Equation (18), and consequently the elastic solution in the vicinity of the pre-existing crack tip, Γ_c, are derived by relating the outer and inner expansions in a common region where both approximations accurately represent the actual solution. In that region, the so-called matching conditions are applied,

$$F_0(l)V_0(y_1, y_2) \approx U(0, 0), \quad \text{when } \rho \to \infty, \tag{19}$$

$$F_1(l)V_1(y_1, y_2) \approx K_I l^\lambda \rho^\lambda u(\theta), \quad \text{when } \rho \to \infty, \tag{20}$$

where $\rho = \sqrt{y_1^2 + y_2^2}$ and $\approx$ means "behave like". Hence, it can be set

$$F_0(l) = 1, \quad V_0(y_1, y_2) \approx U(0, 0), \quad \text{when } \rho \to \infty, \tag{21}$$

$$F_1(l) = K_I l^\lambda, \quad V_1(y_1, y_2) \approx \rho^\lambda u(\theta), \quad \text{when } \rho \to \infty, \tag{22}$$

The expression in Equation (18) is a good approximation of the real solution $U(x_1, x_2)$ in the vicinity of the crack tip. To obtain the solution $V_1(y_1, y_2)$, the finite element method is applied in a circular domain whose dimensions are much larger (in this case, $R = 400\,\mu\text{m}$) than those of the internal domain described in Figures 3 and 4. The element size in the vicinity of the pre-existing crack tip Γ_c is sufficiently small to ensure numerical convergence, with a size of $0.008\,\mu\text{m}$. On the boundary of the domain, a prescribed displacement is applied as a boundary condition, as shown in Figure 5.

Figure 5 Schematic of the numerical problem.

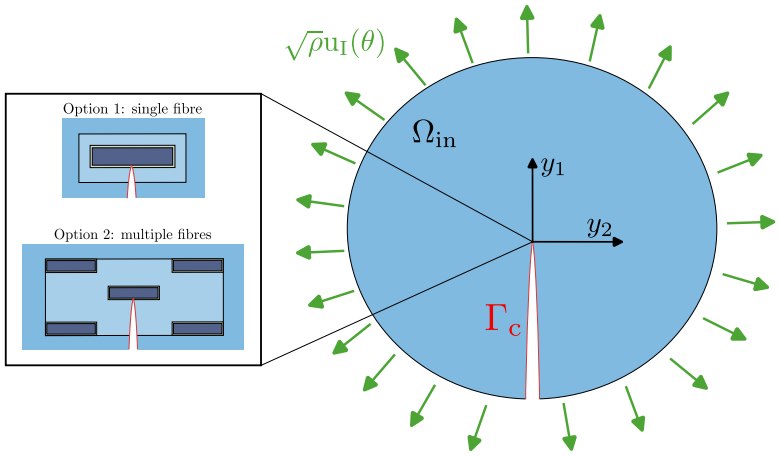

Once the elastic solution is obtained, the two CC conditions, summarised in Equations (1) and (5), are applied, yielding

$$K_I(s) \geqslant \frac{\sqrt{l}\sigma_c(\hat{s})}{\sigma(\hat{s})}, \tag{23}$$

$$K_I(s) \geqslant \sqrt{\frac{G_c(\hat{\delta l})}{-\frac{\Delta\Pi_p}{\hat{\delta l}}}}. \tag{24}$$

The apparent fracture toughness of the composite, denoted as K_{IC}^{app}, corresponds to the minimum value of $K_I(s)$ that satisfies both conditions of the Coupled Criterion, as summarised in Equations (23) and (24). In Equation (23), the tensile stress $\sigma(\hat{s})$ is obtained as

$$\sigma(\hat{s}) = \frac{1}{\sqrt{l}}\nabla_y V_1(y_1, y_2) \tag{25}$$

if the inner domain is built considering the length of the fibre l or

$$\sigma(\hat{s}) = \frac{1}{\sqrt{t}}\nabla_y V_1(y_1, y_2) \tag{26}$$

if the inner domain is built considering the diameter of the fibre t. The term ∇_y is the gradient operator with respect to the variables y_1, y_2. As explained in (Jiménez-Alfaro and Leguillon 2022), the increment in potential energy $\Delta\Pi_p$ is the one directly obtained from the inner problem of solution $V_1(y_1, y_2)$.

Finally, note that the problem is solved under the assumption of plane strain elasticity to estimate fracture toughness. While this simplification offers practical advantages, it may not fully capture the complexities of the real material. Given that the fibres have a round cross-section, their thickness in the perpendicular direction is considerably smaller than their length, introducing limitations to the model's representativeness. Consequently, certain phenomena, such as crack propagation around the fibres, cannot be accurately represented. Nevertheless, despite these constraints, the model provides a reliable first estimate of fracture toughness that aligns well with experimental data, as will be demonstrated in this section.

4 Results and discussions

This section presents the key results obtained from the application of the numerical tool described in Section 3.2 considering the material outlined in Section 3.1. The effect of various geometric parameters of the composite is analysed. Section 4.1 explores the influence of fibre size, proposing a configuration that optimises the fracture toughness of the composite. Section 4.2 investigates the impact of fibre volume fraction, as well as the changes in fracture properties that may arise from including or excluding an intermediate interface between the fibre and the matrix. Additionally, the effect of fibre spacing on fracture toughness is examined. Finally, Section 4.3 compares the two models proposed in Section 3.2, the single-fibre model and the multi-fibre model, with results compared to existing experimental data in the literature in Section 4.4.

4.1 Influence of the size of the fibre

In this section, we examine the influence of two variables: the length l and the diameter t of the fibre. The analysis is conducted for **Material 2**, as described in Section 3.1, using the multi-fibres model detailed in Figure 4. Only two possible paths for the propagation of the pre-existing crack, Γ_c, are analysed, as outlined in Section 3.2: crack penetration into the fibre, and lateral deflection through the interphase. Examples of the two crack paths are represented below in Figures 10 and 12. These are referred to as toughening mechanisms, as they are expected to enhance the fracture toughness of the composite compared to that of the matrix alone. The predominant mechanism — i.e., the one that governs crack propagation — will be the one associated with the lowest calculated value of the apparent fracture toughness $K_{\mathrm{IC}}^{\mathrm{app}}$.

Figure 6 shows the evolution of the apparent fracture toughness, $K_{\mathrm{IC}}^{\mathrm{app}}$, with respect to t, where the chosen range $t = 3\,\mu\mathrm{m}$ to $54\,\mu\mathrm{m}$ is based on the data provided in Section 3.1. For very thin fibres, it can be observed that penetration governs the failure, whereas for thicker fibres, the predominant mechanism is deflection. This suggests that when the fibre is thicker, the interphase acts as a mechanical fuse, causing the crack to deflect through the interphase. Note that a lower $K_{\mathrm{IC}}^{\mathrm{app}}$ is directly associated with a lower failure load, and therefore, the dominant failure mechanism is the one with the lowest $K_{\mathrm{IC}}^{\mathrm{app}}$. The transition from penetration to deflection occurs for t in the range $15\,\mu\mathrm{m}$ to $25\,\mu\mathrm{m}$. This explains the experimental observations of fibre deflection when the interphase is present, as the fibre diameter is sufficiently large to favour this mechanism (see (Legerstee 2022)). Furthermore, a larger fibre diameter results in a higher fracture toughness for the composite, with the maximum enhancement of $K_{\mathrm{IC}}^{\mathrm{app}} = 1.38 K_{\mathrm{IC}}^{\mathrm{m}}$ occurring at $t = 54\,\mu\mathrm{m}$ (the maximum diameter in the range considered), corresponding to $K_{\mathrm{IC}}^{\mathrm{app}} = 3.34\,\mathrm{MPa}\sqrt{\mathrm{m}}$.

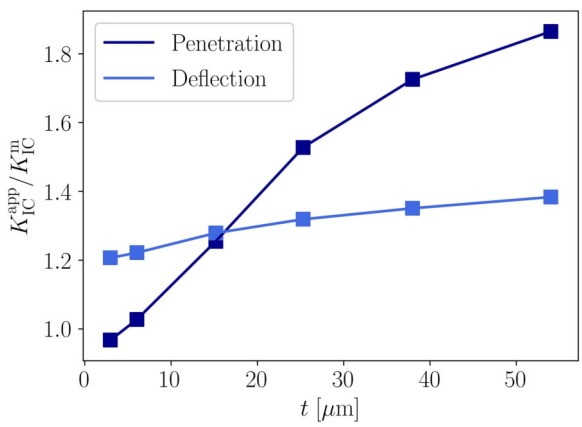

Figure 6 Effect of the fibre diameter t on the apparent fracture toughness of the composite $K_{\mathrm{IC}}^{\mathrm{app}}$ for a fibre volume fraction $V_f = 10\%$ and a fibre length $l = 152\,\mu\mathrm{m}$.

On the other hand, Figures 7 and 8 show the evolution of $K_{\mathrm{IC}}^{\mathrm{app}}$ with respect to the fibre length, l, for two different diameters: $t = t_{\mathrm{avg}} = 16.67\,\mu\mathrm{m}$ and $t = 25\,\mu\mathrm{m}$. The range selected for l is based on the data provided in Section 3.1. First, it can be observed that l does not change the predominant mechanism, which remains penetration for $t = t_{\mathrm{avg}} = 16.67\,\mu\mathrm{m}$ and deflection for $t = 25\,\mu\mathrm{m}$. Therefore, it can be concluded that the predominant mechanism mainly depends on

the fibre diameter. However, l does influence the apparent fracture toughness, with higher values observed when $l \approx t$. Moreover, Figures 7 and 8 show that for very long fibres, the influence of l on $K_{\mathrm{IC}}^{\mathrm{app}}$ is significantly reduced. Interestingly, in the case of $t = 25\,\mu\mathrm{m}$, the apparent fracture toughness for penetration and deflection mechanisms becomes quite similar when considering very short fibres. It is worth noting that the slight non-monotonic variation of $K_{\mathrm{IC}}^{\mathrm{app}}$ is due to the reduced scale of the plot and remains below 3 %, likely caused by minor numerical fluctuations.

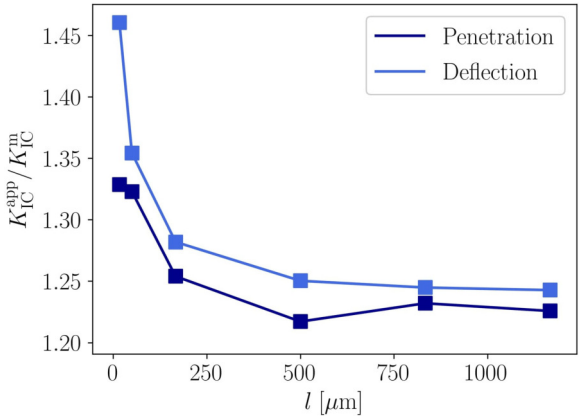

Figure 7 Effect of the fibre length l on the apparent fracture toughness of the composite $K_{\mathrm{IC}}^{\mathrm{app}}$ for a fibre volume fraction $V_f = 10\,\%$ and a fibre diameter $t = 16.67\,\mu\mathrm{m}$.

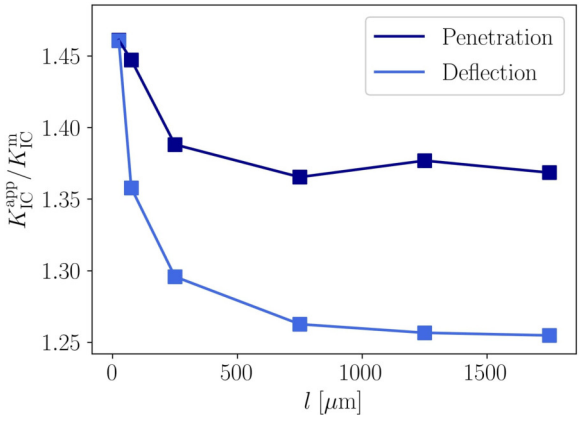

Figure 8 Effect of the length of the fibre l on the apparent fracture toughness of the composite $K_{\mathrm{IC}}^{\mathrm{app}}$ for a volume fraction of fibres $V_f = 10\,\%$ and a thickness of the fibre $t = 25\,\mu\mathrm{m}$.

In conclusion, the fibre diameter plays a major role in determining the predominant toughening mechanism observed in the composite, although both l and t influence $K_{\mathrm{IC}}^{\mathrm{app}}$, which increases when l is close to t. Consequently, square fibres represent the most effective configuration for increasing $K_{\mathrm{IC}}^{\mathrm{app}}$. When $l \approx t$, they become more robust and resistant to penetration, resulting in the highest values of $K_{\mathrm{IC}}^{\mathrm{app}}$. For this reason, Figure 9 represents the evolution of $K_{\mathrm{IC}}^{\mathrm{app}}$ with respect to the fibre size for $t = l$. First, it can be observed that $K_{\mathrm{IC}}^{\mathrm{app}}$ increases with increasing l. Moreover, for small fibres, the predominant mechanism is penetration, whereas for larger fibres, the crack may deflect through the interphase. It is also evident that $K_{\mathrm{IC}}^{\mathrm{app}}$ becomes independent of t for very small fibres in the deflection mechanism. This is because the energy condition of the Coupled Criterion (CC), which does not depend on the fibre size, governs the failure. An example is shown in Figures 11(a) and 12(a), where the CC point is governed by the minimum of the energy condition for a small fibre and the cross point between the stress and the energy condition for a large fibre.

To illustrate the case of deflection for small fibre lengths, an example of the application of the CC in these cases is shown in Figure 10, where the curves of the energy and stress conditions are presented, along with the deformed shape after failure. Note that the crack increment (referred to as the nucleation length in the framework of Finite Fracture Mechanics) is shorter than the length of the interphase, explaining why the crack is arrested before reaching the fibre corner.

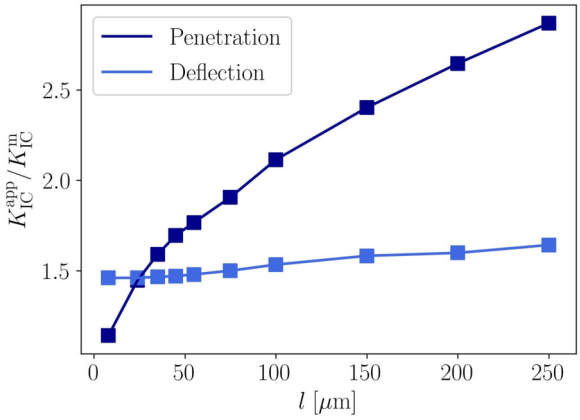

Figure 9 Effect of the fibre length and diameter on the apparent fracture toughness of the composite K_{IC}^{app} for a fibre volume fraction $V_f = 10\,\%$ when $l = t$.

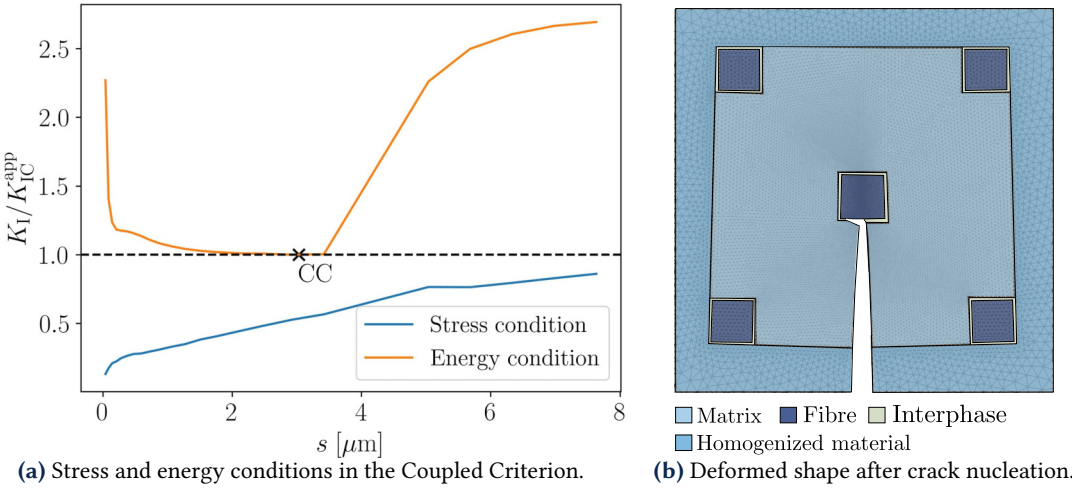

(a) Stress and energy conditions in the Coupled Criterion. **(b)** Deformed shape after crack nucleation.

Figure 10 Application of the Coupled Criterion for the case of deflection in the optimal configuration $l = t$, for the volume fraction of fibres $V_f = 10\%$, and $l = t = 8\,\mu$m.

If $t > 25\,\mu$m in Figure 9, the apparent fracture toughness of the composite, K_{IC}^{app}, begins to increase with growing t in both the deflection and penetration cases. Both situations correspond to conventional cases, where the CC point is the intersection of the energy condition and the stress condition, as shown in Figures 11 and 12 for deflection and penetration, respectively. Notice that, due to the small newly created crack length, we have represented only the vicinity of one fibre in the deformed shape, although the multi-fibre model has been applied.

4.2 Influence of other design parameters

In this section, the influence of other design parameters is studied, such as the fibre volume fraction, the interface effect, and the distance between fibres. The **Material 2** and the multi-fibre model are used unless otherwise stated. Throughout this section, a fibre with $t = l = 17\,\mu$m is considered as the object of study. First, Figure 13 illustrates the influence of V_f on K_{IC}^{app}. The values $V_f = 5$, 10, and 20% correspond to the range obtained statistically in (Legerstee 2022). In addition, the value $V_f = 40\%$ has been proposed to study the effect of saturating the composite with more fibres, although it is purely a numerical model, as it is unknown whether such a high fibre volume fraction is feasible in practice. For $V_f = 5\% - 20\%$, there is little variation in K_{IC}^{app}, with a maximum increase with respect to K_{IC}^{m} of 35% for penetration and 49% for deflection. However, when considering a higher fibre volume fraction, such as $V_f = 40\%$, the fracture toughness of the composite increases 46% for penetration and 52% for deflection with respect to K_{IC}^{m}.

The reason of the high volume fraction effect can be explained by the Figure 14 illustrating the geometry of the multi-fibre model for different values of V_f. As the volume fraction increases, the

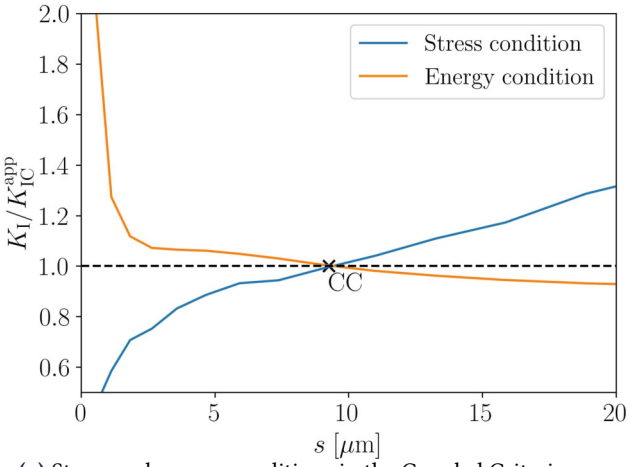

(a) Stress and energy conditions in the Coupled Criterion.

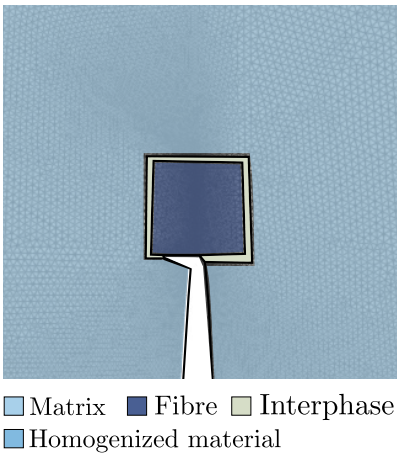

(b) Deformed shape after crack nucleation.

Figure 11 Application of the Coupled Criterion for the case of deflection in the optimal configuration $l = t$, for a fibre volume fraction $V_f = 10\%$, and $l = t = 100\,\mu$m.

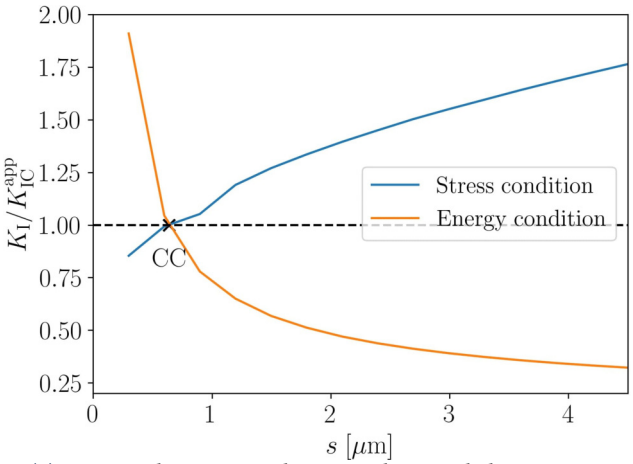

(a) Stress and energy conditions in the Coupled Criterion.

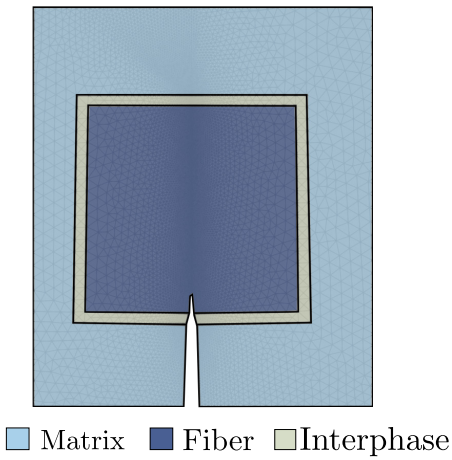

(b) Deformed shape after crack nucleation.

Figure 12 Application of the Coupled Criterion for the case of penetration in the optimal configuration $l = t$, for a fibre volume fraction $V_f = 10\%$, and $l = t = 100\,\mu$m.

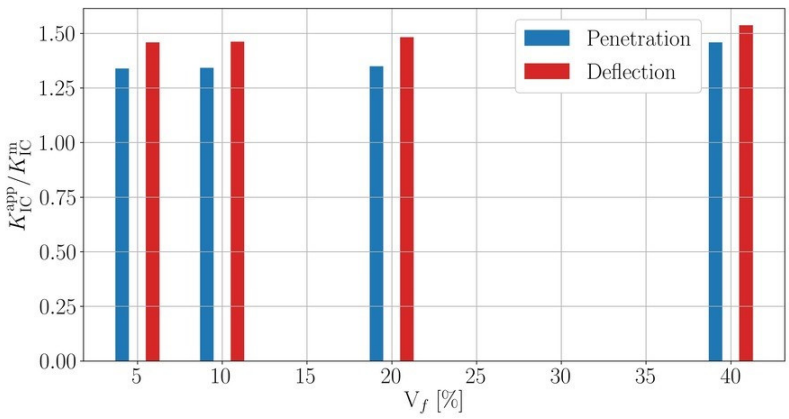

Figure 13 Effect of the fibre volume fraction V_f on the apparent fracture toughness of the composite K_{IC}^{app} for $t = l = 16.67\,\mu$m.

distance between the fibres decreases, that can make extra interactions between fibres allowing higher fracture toughness.

The influence of the interphase in the composite is studied and depicted in Figure 15, where the apparent fracture toughness of the composite, K_{IC}^{app}, is shown as a function of the fibre diameter t for both penetration and deflection when **Material 1** is considered, i.e., when a strong interface between the matrix and the fibre is present. It can be observed that K_{IC}^{app} in the case

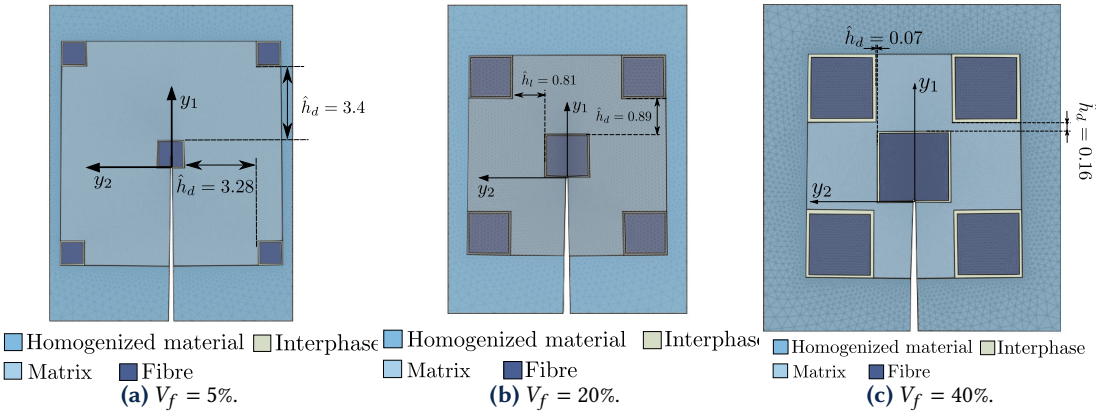

(a) $V_f = 5\%$. **(b)** $V_f = 20\%$. **(c)** $V_f = 40\%$.

Figure 14 Geometries of the multi-fibre model for different fibre volume fraction values.

of deflection increases significantly compared to the case where the interphase is included, making penetration the predominant mechanism, regardless of the fibre diameter. This explains the experimental observation that when the interphase is removed, penetration becomes the dominant damage mechanism, regardless of fibre size, see (Legerstee 2022).

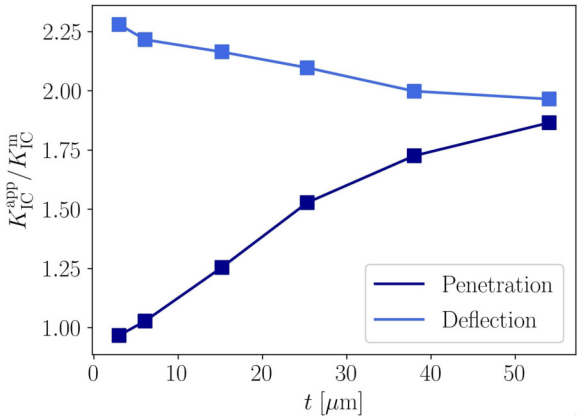

Figure 15 Effect of the fibre diameter t on the apparent fracture toughness of the composite, K_{IC}^{app}, for a fibre volume fraction of $V_f = 10\%$ and a fibre length of $l = 152\,\mu$m, considering no interphase.

Figure 16 shows K_{IC}^{app} for the cases with (**Material 2**) and without interphase (**Material 1**). For small-diameter fibres, where the predominant mechanism is penetration, there is no difference between the interphase and non-interphase cases. However, for larger fibre diameters, K_{IC}^{app} is greater in the non-interphase case because the interphase causes a crack propagation by deflection easier. Note that this observation appears to contradict experimental measurements from (Legerstee 2022), as shown in Table 2. This is because the measurement of K_{IC}^{app} in experiments is based on the total failure of the structure, which is related to crack propagation until complete failure occurs. When the interphase between the fibre and matrix is included, the crack meanders and delays the moment of total failure, thereby increasing the overall load. This effect cannot be captured by our numerical tool, which only measures the interaction between the crack and a single fibre as a necessary criterion for initiation of the crack propagation.

4.3 Multiple versus single fibre model

In Figures 17 and 19, K_{IC}^{app} is shown as a function of t for both the multi-fibre and single-fibre models, for two different values of $V_f = 10\%$ and 40%, considering only the deflection case (similar conclusions are obtained for the penetration case, but these have been omitted for simplicity). For $V_f = 40\%$, the maximum difference reaches 4.15%, which is greater than for $V_f = 10\%$, where the maximum difference is 1.5%. In other words, the larger the volume fraction, the greater the difference between the two models, although the difference remains relatively small. As observed in Figure 17, the distinction between the multi fibres and single fibre models becomes significant

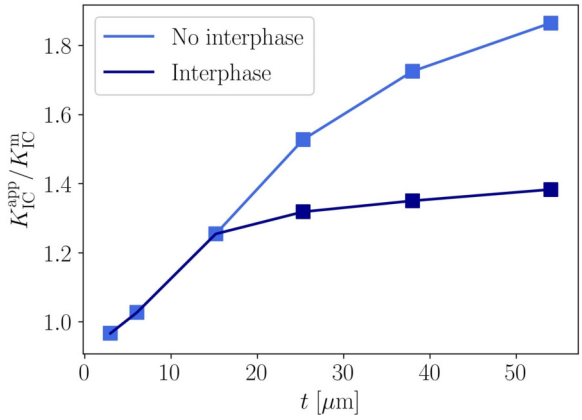

Figure 16 Comparison of K_{IC}^{app} with respect to t with and without the interphase for $V_f = 10\%$ and $l = t$.

for smaller fibre sizes, where the influence of neighbouring fibres - accounted for only in the multi-fibre model - is increasingly more pronounced.

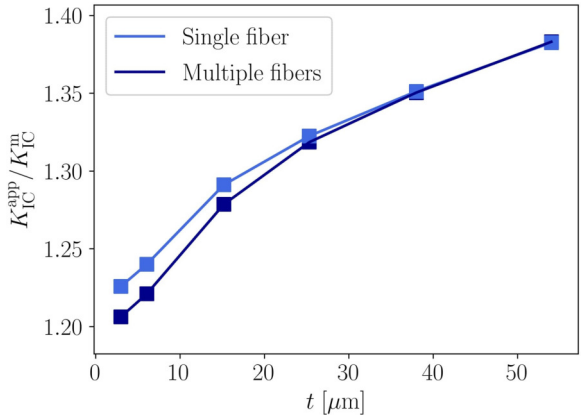

Figure 17 Comparison between the single- and the multi-fibre model in the deflection case, for $l = l_{avg} = 152\,\mu$m. Case of $V_f = 10\%$.

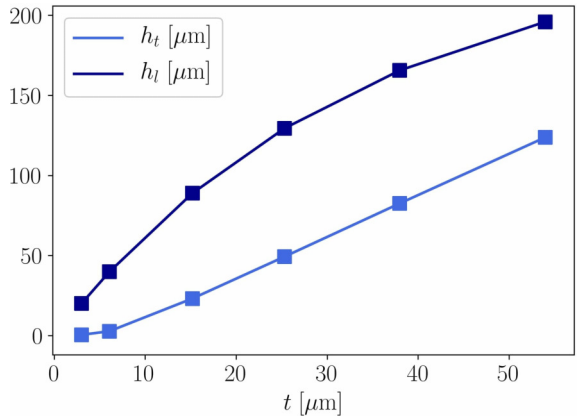

Figure 18 Evolution of distances h_l and h_t for $l = l_{avg} = 152\,\mu$m. Case of $V_f = 10\%$.

In general, the difference between the multi-fibre model and the single-fibre model will be greater when the neighbouring fibres have a more significant effect on the central fibre, which is the one directly interacting with the crack. For the same V_f, a smaller distance between fibres in the multi-fibre model (h_l and h_t) will increase the influence of the neighbouring fibres, thus amplifying the difference between the two models. This is clearly illustrated in Figure 18, for $V_f = 10\%$ and $l = 152\,\mu$m, where h_l and h_t are reduced for smaller values of t. The maximum difference between the models is observed in this region of smaller t.

However, this is not observed in Figure 19, where it can be seen that the difference between

the two models increases with growing t for $V_f = 40\%$. Looking at Figure 20, where h_l and h_t are represented, it is observed that although the distance h_l increases as t increases, the distance h_t remains almost constant except for the last point where it is slightly higher. This varies aspect ratio between the two distances representing variations of fibre stacking. Additionally, h_t is zero. For this reason, the difference between the two models may be motivated by the distance between the fibres and their stacking format of fibres, which will be more pronounced if we consider more fibres.

Finally, in Figure 21, the influence of the distance h_l is analysed. Previously, we used the minimisation of surface area as a criterion to calculate h_l and h_t in the heterogeneous microstructure of the inner domain. However, this criterion lacks a physical explanation and may not be representative. For this reason, the influence of the distance between fibres is studied by selecting a wide range of h_l values and defining h_t so that the constraints in Equations (13) to (16) are satisfied. It is observed that for negative values of this distance, which would imply that fibres are interleaved in the microstructure, there is a jump in the fracture toughness. The improvement in fracture toughness due to an interleaved fibre structure is not surprising. For instance, in construction, brick structures often utilise a technique known as "stretcher bond", where the bricks are interleaved to prevent the joints from aligning, thereby enhancing the strength of the wall. It is important to note that this effect can only be observed when considering a multi-fibre model and not with the previously presented single fibre model.

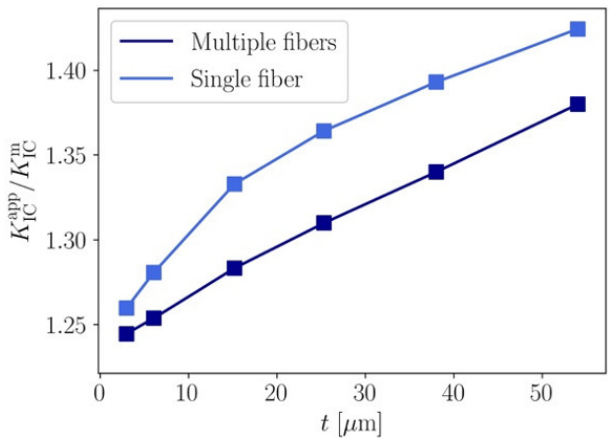

Figure 19 Comparison between the single fibre and the multi-fibre model in the deflection case, for $l = l_{avg} = 152\,\mu$m. Case of $V_f = 40\%$.

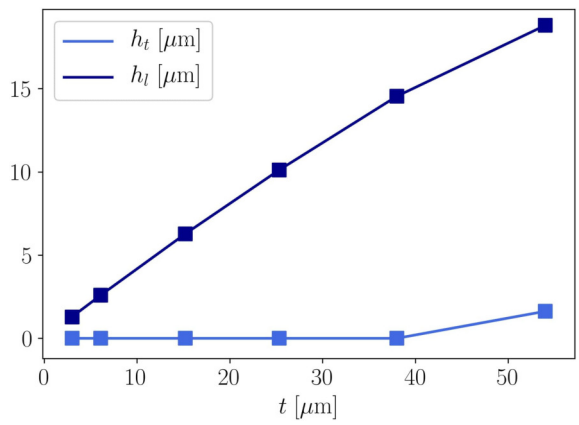

Figure 20 Evolution of distances h_l and h_t for $l = l_{avg} = 152\,\mu$m. Case of $V_f = 40\%$.

Two examples of the geometries obtained for $h_l > 0$ and $h_l > 0$ are shown in Figures 22 and 23. The parameter h_t is obtained to fulfil the geometrical restrictions in Equations (13) to (16).

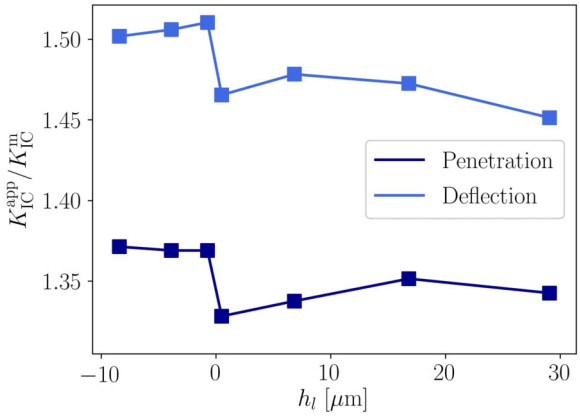

Figure 21 Influence of the distance between fibres h_l on the apparent fracture toughness of the composite K_{IC}^{app} for $V_f = 10\%$ and $l = t = 17\,\mu$m, considering the interphase (**Material 2**). .

Figure 22 Fibre distribution in the inner domain with $h_l > 0$.

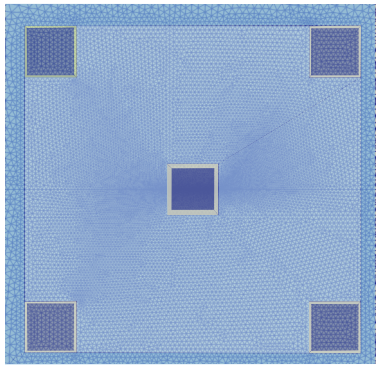

Figure 23 Fibre distribution in the inner domain with $h_l < 0$.

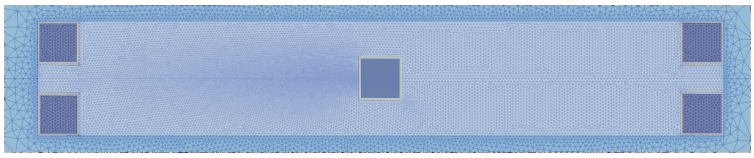

4.4 Comparison to experiments

Finally, it is challenging to validate this model through a precise comparison with the experimental results shown in Table 2, as the specimens contain fibres of various sizes and aspect ratios. Nevertheless, the range numerically estimated for K_{IC}^{app}, considering the average l_{avg}, $V_f = 10\%$, and $t = 3{-}54\,\mu$m, is $K_{IC}^{app} = [2.34{-}4.50]\,\text{MPa}\sqrt{\text{m}}$ with the interphase, $K_{IC}^{app} = [2.34{-}3.34]\,\text{MPa}\sqrt{\text{m}}$ without the interphase. The results are similar to the range obtained experimentally without an interphase, $K_{IC}^{app} = [2.80 - 4.40]\,\text{MPa}\sqrt{\text{m}}$, although it differs more from the range obtained in (Legerstee 2022) with the interphase, $K_{IC}^{app} = [3.87 - 6.32]\,\text{MPa}\sqrt{\text{m}}$. This discrepancy may be attributed to several factors, including the fact that dynamic effects of the interface were not considered here in our numerical approach, and some of the mechanical properties used for the interphase were those of BN instead of PyC, which is the material used in the experiments. As mentioned in Section 3.1, the properties of BN are the ones mentioned in (Legerstee 2022) to describe the interphase for confidential reasons. Moreover, 3D effects and stochastic features (fibre orientation, materials properties, defects) may lead to quantitative discrepancies. It is important to highlight that only crack initiation from the pre-existing crack is considered here, not the crack propagation across a distance larger to crack initiation length.

However, qualitative conclusions obtained in experiments are also observed using this computational tool. When considering the interphase, a very small diameter of the fibre results in lower K_{IC}^{app}, and the failure mechanism is penetration. However, when fibres have larger t, they are more robust and difficult to penetrate, resulting in higher K_{IC}^{app}, and the failure mechanism is deflection, allowing the interface to act as a mechanical fuse. This would explain why experimental observations show fibre deflection when an interphase is present, since the diameter used is sufficiently large to favor this mechanism, according to our numerical

estimations. In case of the system without interface, penetration becomes the dominant damage mechanism, regardless of fibre size. This numerical result is also confirmed experimentally.

Note that, unlike the penetration mechanism, the deflection mechanism causes a much longer crack propagation path, which requires additional energy for the increasing path to failure. Consequently, this must be taken into account for an accurate estimation of $K_{\mathrm{IC}}^{\mathrm{app}}$ based on the deflection mechanism. However, our current numerical model is not yet able to consider this effect. This could be the main reason for the small discrepancy observed without an interphase and the larger discrepancy with an interface between the numerical estimations and experimental results.

5 Conclusions

In this paper, a computational tool for estimating fracture toughness in short-fibre ceramic matrix composites has been developed and applied to an industrial composite material. The following key findings are highlighted:

- The fracture toughness estimated by the computational tool was thoroughly validated by comparing them with experimental data, both qualitatively and quantitatively.
- The fibre volume fraction effect on the $K_{\mathrm{IC}}^{\mathrm{app}}$ can be negligible when lower values up to $V_f = 20\%$, are considered, while a very high value of volume fraction, such as $V_f = 40\%$, increases the $K_{\mathrm{IC}}^{\mathrm{app}}$ significantly. It is because of the effect of interactions between fibres.
- The predominant failure mechanism is primarily influenced by the presence of the interphase and the fibre size. When the interphase is present, smaller fibre diameters result in lower $K_{\mathrm{IC}}^{\mathrm{app}}$, with penetration being the dominant failure mechanism. In contrast, larger fibre diameters promote fibre deflection, allowing the interphase to act as a mechanical fuse, which is same as experimental observation. Conversely, when the interphase is removed, penetration becomes the dominant damage mechanism, regardless of fibre size, as observed experimentally. Notice that this computational tool could be used to determine the properties of the interphase that govern the competition between penetration and deflection.
- There is not a significant difference between the multi-fibre and the single fibre model if there is no change of fibre stacking represented by the ratio between the two distances between fibres, h_l and h_t. That is why, for general estimations, the use of the single fibre model is proposed as it has a lower computational complexity. For the same level of refinement, it requires approximately half of the number of elements.
- Square fibres represent the most effective configuration for increasing $K_{\mathrm{IC}}^{\mathrm{app}}$. When $l \approx t$, they become more robust and resistant to penetration, resulting in the highest values of $K_{\mathrm{IC}}^{\mathrm{app}}$. It is important to note that the spatial distribution of fibres, and therefore the statistical probability of the crack encountering a fibre, has not been included in this analysis. The optimal configuration could change if this effect is considered. Moreover, an additional condition should be considered to ensure that the crack does not propagate exclusively through the matrix. This can be addressed by imposing that the probability of a crack encountering a fibre is greater than 50%, i.e., $3^l/\hat{a}_l > 0.5$.
- Additionally, the intercalation of fibres also has an effect on $K_{\mathrm{IC}}^{\mathrm{app}}$, which can increase approximately 4%.
- Finally, no initial stress field is considered, which is likely to originate from the processing, e.g., residual stresses. This could be included in the model as a future work. An example is shown in (Jiménez-Alfaro and Leguillon 2023).

A Appendix

Two distinct numerical simulations are required. The first is used to compute the tensile stress field that defines the stress state in the CC, and it is performed on a configuration prior to any crack nucleation (i.e., only including the pre-existing crack within the inner domain). Subsequently, a series of simulations are carried out to evaluate the increment in potential energy for various crack lengths. This is done by progressively releasing nodes along the crack path and calculating the difference in potential energy between the cracked and uncracked configurations. The same finite element mesh is employed for both the initial undamaged simulation and all

subsequent cracked simulations, ensuring numerical consistency throughout. The resulting potential energy increment is then used to define the energy-based fracture criterion. The mesh crack size in the interphase is 0.003 µm, whereas in the fibre is 0.005 µm. In the matrix the mesh size next to the tip of the pre-existing crack is 0.007 µm. In the outer bound of the boundary, see Figure 5 the mesh size is around 37 µm. Although the mesh gradient is huge, the domain has also a big size, so the transition is smooth, see Figure A.1 for a example where $V_f = 30\%$, and the aspect ratio between the length and the diameter of the fibre is 15.

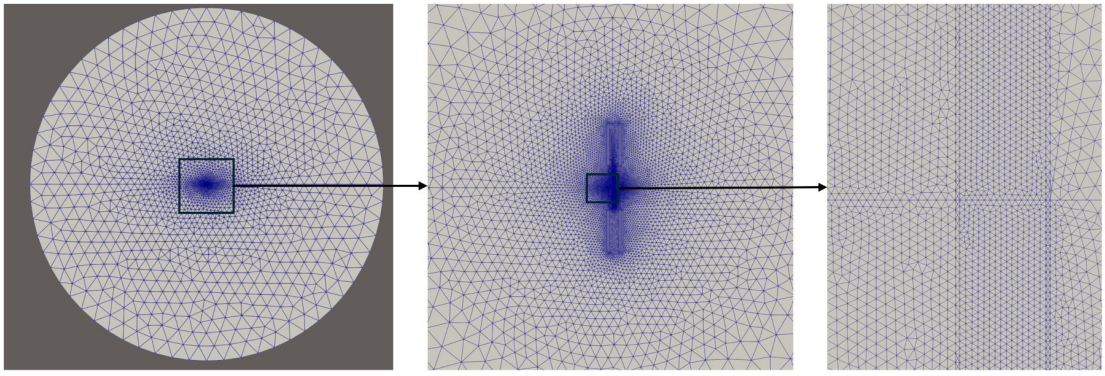

Figure A.1 Example of a mesh in the simulation.

References

Barsoum, M. W., P. Kangutkar, and A. Wang (1992). Matrix crack initiation in ceramic matrix composites Part I: Experiments and test results. *Composites Science and Technology* 44(3):257–269. [DOI].

Dhanasekar, S., A. T. Ganesan, T. L. Rani, V. K. Vinjamuri, M. Nageswara Rao, E. Shankar, Dharamvir, P. S. Kumar, and W. Misganaw Golie (2022). A Comprehensive Study of Ceramic Matrix Composites for Space Applications. *Advances in Materials Science and Engineering* 2022:1–9. [DOI], [OA].

Doitrand, A., R. Henry, H. Saad, S. Deville, and S. Meille (2020). Determination of interface fracture properties by micro- and macro-scale experiments in nacre-like alumina. *Journal of the Mechanics and Physics of Solids* 145:104143. [DOI], [OA].

Donald, I. W. and P. W. McMillan (1976). Ceramic-matrix composites. *Journal of Materials Science* 11(5):949–972. [DOI].

Duminy, T., R. Henry, J. Adrien, A. Doitrand, and S. Meille (2023). Anisotropic fracture in nacre-like alumina. *Theoretical and Applied Fracture Mechanics* 123:103710. [DOI], [OA].

European Commission (2019). *The European Green Deal*. COM.

Gavalda-Diaz, O., E. Saiz, J. Chevalier, and F. Bouville (2025). Toughening of ceramics and ceramic composites through microstructure engineering: A review. *International Materials Reviews* 70(1):3–30. [DOI], [OA].

Jiménez-Alfaro, S. and D. Leguillon (2022). Modelling of glass matrix composites by the Coupled Criterion and the Matched Asymptotics approach. The role of a single platelet. *Theoretical and Applied Fracture Mechanics* 122:103650. [DOI], [OA].

Jiménez-Alfaro, S. and D. Leguillon (2023). Modelling of glass matrix composites by the Coupled Criterion and the Matched Asymptotic Approach. The effect of residual stresses and volume fraction. *Theoretical and Applied Fracture Mechanics* 128:104112. [DOI], [OA].

Jiménez-Alfaro, S., I. G. García, and A. Doitrand (2025). Review of the matched asymptotic approach of the coupled criterion. *Comptes Rendus. Mécanique* 353(G1):339–357. [DOI], [OA].

Jiménez-Alfaro, S. and D. Leguillon (2021). Finite fracture Mechanics at the micro-scale. Application to bending tests of micro cantilever beams. *Engineering Fracture Mechanics* 258. [DOI], [OA].

Legerstee, Y. (2022). Caractérisation et modélisation du comportement thermomécanique de composites à matrice céramique renforcés par des fibres courtes. French. PhD thesis. France: Université de Bordeaux. [OA].

Leguillon, D., E. Martin, O. Ševeček, and R. Bermejo (2015). Application of the coupled stress-energy criterion to predict the fracture behaviour of layered ceramics designed with internal compressive stresses. *European Journal of Mechanics - A/Solids* 54:94–104. [DOI], [OA].

Leguillon, D. (2002). Strength or toughness? A criterion for crack onset at a notch. *European Journal of Mechanics - A/Solids* 21(1):61–72. [DOI], [OA].

Leguillon, D., E. Martin, O. Sevecek, and R. Bermejo (2018). What is the tensile strength of a ceramic to be used in numerical models for predicting crack initiation? *International Journal of Fracture* 212(1):89–103. [DOI], [OA].

Martin, E., D. Leguillon, O. Sevecek, and R. Bermejo (2018). Understanding the tensile strength of ceramics in the presence of small critical flaws. *Engineering Fracture Mechanics* 201:167–175. [DOI], [OA].

Martin, E., P. Peters, D. Leguillon, and J. Quenisset (1998). Conditions for matrix crack deflection at an interface in ceramic matrix composites. *Materials Science and Engineering: A* 250(2):291–302. [DOI], [OA].

Martin, E., D. Leguillon, and C. Lacroix (2001). A revisited criterion for crack deflection at an interface in a brittle bimaterial. *Composites Science and Technology* 61(12):1671–1679. [DOI], [OA].

Ohnabe, H., S. Masaki, M. Onozuka, K. Miyahara, and T. Sasa (1999). Potential application of ceramic matrix composites to aero-engine components. *Composites Part A: Applied Science and Manufacturing* 30(4):489–496. [DOI], [OA].

Papšík, R., O. Ševeček, A.-K. Hofer, I. Kraleva, J. Kreith, and R. Bermejo (2023). Prediction of edge and tunnelling crack formation in layered ceramics using a stress-energy fracture criterion. *Journal of the European Ceramic Society* 43(7):2928–2934. [DOI], [OA].

Papšík, R., O. Ševeček, J. Schlacher, and R. Bermejo (2024). Prediction of thermal shock induced cracking in multi-material ceramics using a stress-energy criterion. *Engineering Fracture Mechanics* 303:110121. [DOI], [OA].

Picard, D., D. Leguillon, and C. Putot (2006). A method to estimate the influence of the notch-root radius on the fracture toughness measurement of ceramics. *Journal of the European Ceramic Society* 26(8):1421–1427. [DOI], [OA].

Ševeček, O., M. Kotoul, D. Leguillon, E. Martin, and R. Bermejo (2016). Modelling of edge crack formation and propagation in ceramic laminates using the stress-energy coupled criterion. *Engineering Fracture Mechanics* 167:45–55. [DOI], [OA].

Weißgraeber, P., D. Leguillon, and W. Becker (2016). A review of Finite Fracture Mechanics: crack initiation at singular and non-singular stress raisers. *Archive of Applied Mechanics* 86(1-2):375–401. [DOI], [OA].

Williams, M. L. (1952). Stress Singularities Resulting From Various Boundary Conditions in Angular Corners of Plates in Extension. *Journal of Applied Mechanics* 19(4):526–528. [DOI], [OA].

Open Access This article is licensed under a Creative Commons Attribution 4.0 International License, which permits use, sharing, adaptation, distribution and reproduction in any medium or format, as long as you give appropriate credit to the original author(s) and the source, provide a link to the Creative Commons license, and indicate if changes were made. The images or other third party material in this article are included in the article's Creative Commons license, unless indicated otherwise in a credit line to the material. If material is not included in the article's Creative Commons license and your intended use is not permitted by statutory regulation or exceeds the permitted use, you will need to obtain permission directly from the authors–the copyright holder. To view a copy of this license, visit creativecommons.org/licenses/by/4.0.

Authors' contributions S. Jiménez-Alfaro: edition, calculation. H.J. Chang: supervison, calculation, edition. D. Leguillon: supervision, calculation. S. Denneulin: supervision, calculation.

Supplementary Material Available at the permalink 10.5281/zenodo.17534583.

Acknowledgements S. Jimenez-Alfaro acknowledges the Iberdrola Foundation under the Marie Skłodowska-Curie Grant Agreement No 101034297. She also acknowledges the support of the Ministerio de Ciencia e Innovación of Spain for their Juan de la Cierva postdoctoral fellowship under reference JDC2023-050492-I.

Competing interests The authors declare that they have no competing interests.

Journal's Note JTCAM remains neutral with regard to the content of the publication and institutional affiliations.